Titre: Title:	Simulation-based investigation of unsteady flow in near-hub region of a Kaplan turbine with experimental comparison
Auteurs: Authors:	B. G. Mulu, M. J. Cervantes, Christophe Devals, T. C. Vu, & François Guibault
Date:	2015
Type:	Article de revue / Article
Référence: Citation:	Mulu, B. G., Cervantes, M. J., Devals, C., Vu, T. C., & Guibault, F. (2015). Simulation-based investigation of unsteady flow in near-hub region of a Kaplan turbine with experimental comparison. Engineering Applications of Computational Fluid Mechanics, 9(1), 139-156. https://doi.org/10.1080/19942060.2015.1004816

URL de PolyPublie: PolyPublie URL:	https://publications.polymtl.ca/5040/
Version:	Version officielle de l'éditeur / Published version Révisé par les pairs / Refereed
Conditions d'utilisation: Terms of Use:	CC BY

Titre de la revue: Journal Title:	Engineering Applications of Computational Fluid Mechanics (vol. 9, no. 1)
Maison d'édition: Publisher:	Taylor & Francis
URL officiel: Official URL:	https://doi.org/10.1080/19942060.2015.1004816
Mention légale: Legal notice:	© 2015 The Author(s). Published by Taylor & Francis.This is an Open Access article distributed under the terms of the Creative Commons Attribution License (http://creativecommons.org/licenses/by/4.0/), which permits unrestricteduse, distribution, and reproduction in any medium, provided the original work is properly cited.
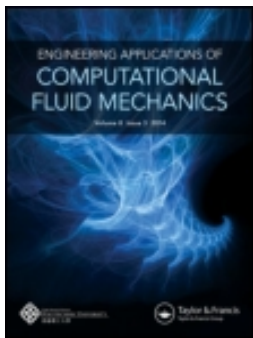
Simulation-based investigation of unsteady flow in near-hub region of a Kaplan Turbine with experimental comparison

B. G. Mulu, M. J. Cervantes, C. Devals, T. C. Vu & F. Guibault

Taylor & Francis
Taylor & Francis Group

Simulation-based investigation of unsteady flow in near-hub region of a Kaplan Turbine with experimental comparison

B. G. Mulu[a], M. J. Cervantes[b,c]*, C. Devals[d], T. C. Vu[e] and F. Guibault[d]

[a]*Vattenfall Research and Development AB, Laboratorievägen, SE-814 26 Alvkarleby, Sweden;* [b]*Division of Fluid and Experimental Mechanics, Luleå University of Technology, SE-971 87 Luleå, Sweden;* [c]*Department of Energy and Process Engineering, Water Power Laboratory, Norwegian University of Science and Technology, Trondheim, Norway;* [d]*Computer and Software Engineering Department, Ecole Polytechnique de Montréal, Montréal, QC, Canada, H3C 3A7;* [e]*Andritz Hydro Ltd., 6100 TransCanada Hwy, Pointe-Claire, QC, Canada*

This paper presents a detailed comparison of steady and unsteady turbulent flow simulation results in the U9 Kaplan turbine draft tube with experimental velocity and pressure measurements. The computational flow domain includes the guide vanes, the runner and the draft tube. A number of turbulence models were studied, including the standard $k - \varepsilon$, RNG $k - \varepsilon$, SST and SST-SAS models. Prediction of the flow behavior in the conical section of the draft tube directly below the runner cone is very sensitive to the prediction of the separation point on the runner cone. The results demonstrate a significant increase in precision of the flow modeling in the runner cone region by using unsteady flow simulations compare to stage simulation. The prediction of the flow in the runner cone region, however, remains delicate, and no turbulence model could accurately predict the complex phenomena observed experimentally.

Keywords: Kaplan turbine; hydropower; boundary condition; CFD; experimental validation

1. Introduction

Over the last decade, the constant increase in demand for energy has pushed current electric production facilities to their operational limits. In this context, the rehabilitation of aging hydraulic installations often appears as a way to increase the production capacity in a way that is both economically advantageous and socially acceptable. From an engineering design perspective, however, rehabilitation projects carry enormous challenges. Designers must either modify existing components or develop new components that are both highly specific to site operating conditions, and well adapted to existing components, for which replacement cannot be economically justified. An accurate analysis of existing installations, therefore, constitutes a central competitive tool both during feasibility studies, to determine which components should be replaced, as well as during the engineering design phases, to ensure that contractual guarantees can be met. Short design cycle times may impose severe constraints on the acceptable duration of those analyses, and may prevent analysts from resorting to laboratory tests. Even when available, model tests are very expensive and mainly offer integral values such as efficiency and parameters at a limited number of measurement points. Such information is crucial for design validation but is restrictive in its ability to support design optimization. Numerical simulations, on the other hand, provide detailed values everywhere in the computational domain.

The fidelity of flow simulations currently varies from the most inexpensive potential flow models to the highest fidelity LES and DNS simulations. In this spectrum, high fidelity unsteady, turbulent viscous flow models constitute a powerful alternative to understand existing turbine characteristics, predict the global system behavior and optimize specific flow regions, offering detailed information over the entire flow field. The current performance of large computer clusters allows for consideration of unsteady Reynolds averaged Navier-Stokes (URANS) simulations in multiple turbine components as the highest level of model fidelity currently available to analysts in production environments. These simulations, however, still fall short in their attempts to capture the full complexity of hydraulic turbine flow. This deficiency, is especially true in axial machines, such as propellers and Kaplan turbines, and is even more obvious when only some components of the turbine are analyzed. There is, consequently, a need to validate the RANS and URANS simulations in axial turbines against precise model measurements carried out in the laboratory.

---

*Corresponding author. Email: michel.cervantes@ltu.se

2. State of the art

Comparisons between numerical simulations and experiments in draft tubes have been carried out for several combinations of components and machine types. The most advanced simulations have been carried out in Francis turbines (Ciocan, Iliescu, Vu, Nennemann, & Avellan, 2007; Vu, Devals, Zhang, Nennemann, & Guibault, 2011a), for instance, as part of the FLINDT project, which took place at Ècole Polytechnique Fédérale de Lausanne (EPFL) and involved several turbine manufacturers. High fidelity RANS simulations, both steady and unsteady, of the runner and draft tube have shown very good agreement between experimental measurements and simulation results. A number of validation cases have also been carried out using Large-Eddy Simulations (LES) for a draft tube downstream a Francis runner (Duprat et al., 2009), and more recently for a whole Francis turbine, including distributor, runner and draft-tube in Su, Li, Li, Wei, and Zhao (2012).

Similar work is currently also underway for propeller machines as part of the Axial-T project conducted at Laval University. Comparisons between model measurements and RANS and URANS simulations in the draft tube cone region of this propeller turbine have highlighted some of the difficulties involved in predicting accurately the flow below the runner in axial machines (Gagnon et al., 2012; Gagnon, Flemming, Qian, Desch Aanes, & Coulson, 2010; Henau et al., 2010; Vu, Koller, Gauthier, & Deschêne, 2011b).

There are, however, few experimental results currently available that allow comparisons in Kaplan turbines, with the notable exception of the Turbine-99 test case (Cervantes, Engström, & Gustavsson, 2005), where the draft tube geometry together with the experimental results have been published describing the flow and the geometry. These experimental results include the velocity inlet boundary conditions immediately after the runner and the velocity profiles in the draft tube cone and diffuser. These results, along with several comparisons using numerical simulations, indicate that the boundary conditions at the draft tube inlet have a large influence on the flow prediction accuracy. Swirling flows that are subject to a strong adverse pressure gradient are difficult to simulate accurately because they are very sensitive. It is important to feed the draft tube with the correct swirl to be able to capture the correct draft tube flow. In addition to the problems associated with the inlet boundary conditions, the flow computation in a Kaplan draft tube is also challenging due to the different flow phenomena appearing simultaneously. The region near the runner cone is of fundamental importance. In this area, a highly unsteady turbulent swirling flow is affected by a strong adverse pressure gradient. Slight variations in the numerical prediction of the flow separation point along the runner cone produces important variations in the flow prediction in the cone region, which may affect the overall performance estimation of the turbine. This problem was investigated numerically by Nilsson (2006), where runner simulations without the draft tube were performed in the Turbine-99 test case. The trailing blade-hub clearance was found to be important in keeping the flow attached to the runner cone because the flow was feeding momentum to the boundary layer. In recent work, Nilsson and Cervantes (2012) have presented unsteady simulations in the Turbine-99 draft-tube using the experimental phase average velocity proposed at the workshop as inlet boundary conditions. From this study, it was concluded that draft-tube alone simulations were very sensitive to the inlet boundary flow resolution, in particular in the region below the hub.

The problems related to this complex flow physics are compounded by the fact that turbulence needs either to be modeled or resolved accurately, and, in the latter case, at an extremely high computational cost. Recently, Galvan, Reggio, and Guibault (2011) investigated the sensitivity of steady-state flow simulations in the Turbine-99 Kaplan draft tube, by comparing several two-equation turbulence models. They concluded that the RNG $k - \varepsilon$ model provided the best agreement with experimental measurements, at the expense, however, of good convergence behavior of the simulations. Similar conclusions were also drawn by Krzemianowski, Banaszek, and Tesch (2011), once again for steady flow simulations. In terms of unsteady flow simulations in Kaplan turbines, most studies have been devoted to the prediction of pressure pulsation at off-design conditions. For instance, Kurosawa and Satou (2006) carried out unsteady flow simulations in a complete Kaplan turbine, but presented no comparison between experimental and simulated velocities. Similarly, Liu, Shao, Wu, and Wu (2008) focused on the comparison of fluctuating pressure signals at the draft-tube wall.

In the current paper a Kaplan turbine model known as Porjus U9 is investigated numerically. Recently, Mulu, Cervantes, Vu, Devals, and Guibault (2011) have investigated the influence of the boundary conditions at the draft tube inlet on the flow prediction accuracy downstream of the Porjus U9 runner using a detailed comparison of the steady RANS simulations and the experimental results at the best efficiency point. The influence of the mesh resolution and turbulence model were investigated, as well as the impact of the flow quantity averaging process at the draft tube inlet. Two types of computations were carried out: the first involved the draft tube alone, and the second computation used stage averaging between the runner and the draft tube. The RANS two-equation eddy-viscosity turbulence models ($k - \varepsilon$, RNG $k - \varepsilon$ and SST) and the Reynolds stress models (SSG and BSL) were used in the study. The computations of the draft tube with the experimental inlet boundary conditions demonstrated the difficulty of the two-equation models to capture the draft tube cone central vortex that is produced by the runner

cone. Two-equation turbulence models predicted an early separation on the runner cone. The Reynolds stress models (RSM) performed satisfactorily and demonstrated the anisotropy of the flow. As for the stage calculations results, they gave the general characteristics of the draft tube flow and were found to be surprisingly insensitive to the turbulence model used. All turbulence models predicted an early separation on the runner cone and over-predicted the size of the draft tube cone central vortex below the runner cone. Furthermore, the effect of the blade wake and the hub-blade clearance were not accurately predicted. Further downstream, the numerical results better matched the experimental results because of numerical diffusion. These results and other investigations using the Porjus U9 draft tube carried out by Petit, Mulu, Nilsson, and Cervantes (2010), Petit, Nilsson, Vu, Manole, and Leonsson (2008), have allowed to determine that unsteady analysis of the turbine, including the guide vanes, the runner and the draft tube, are needed to better capture the complex flow behavior below the runner cone. To the best of the authors' knowledge, up to now, no work has been devoted to the comparison of fully coupled unsteady flow simulations in a Kaplan runner and draft-tube with experiments and the analysis of the near hub velocity field in the presence of jets generated by near-hub blade gap.

This paper presents the URANS simulation results and a detailed comparison with the experimental results of the U9 model turbine at the best efficiency operating point. The computational flow domain includes the guide vanes, the runner and the draft tube. This paper is structured as follows: the next section describes the turbine model, followed by a section describing the numerical models and the evaluation method used. Section 7 presents the results and comparisons, and the paper ends with the discussions and conclusions.

3. Test case

The experimental investigation was performed in a Kaplan turbine model known as Porjus U9. The measurements were made in a draft tube that was built at a 1:3.1 scale model of the prototype turbine. The experiment was conducted under a constant runner blade angle and at the three following loads: the best efficiency point (BEP) and two off-design operating points (part load and high load). The runner angular velocity was 696.3 rpm. The velocities were measured with a two-component LDA technique (Mulu & Cervantes, 2009).

Four Plexiglas windows were used to perform the LDA measurements. The windows were placed at an angular positions a, b, c, and d, with a 90° spacing around the cone circumference. At each angular position three locations (sections I to III) along the vertical direction were investigated. At angular positions a and d, two additional profiles were measured perpendicular to the cone axis (BC in Figure 1), which were used as inlet boundary conditions for the numerical simulations. A detailed description of the test rig and the experimental results can be found in Mulu, Jonsson, and Cervantes (2012) and Jonsson, Mulu, and Cervantes (2012).

The pressure measurements were performed using membrane-type pressure transducers with an accuracy of 0.1%. Several pressure sensors were installed along the draft tube. Twenty taps were mounted in the conical diffuser at four angular positions circumferentially, i.e., at each angular position equally spaced five taps were installed in the vertical direction (Figure 1). The angular positions were the same as the LDA measurement sections (a–d). A total of 13 pressure taps were mounted on the draft tube elbow; seven taps along the inner radius and six taps along the outer radius. A reference pressure tap was located near the outlet of the straight diffuser. L* is
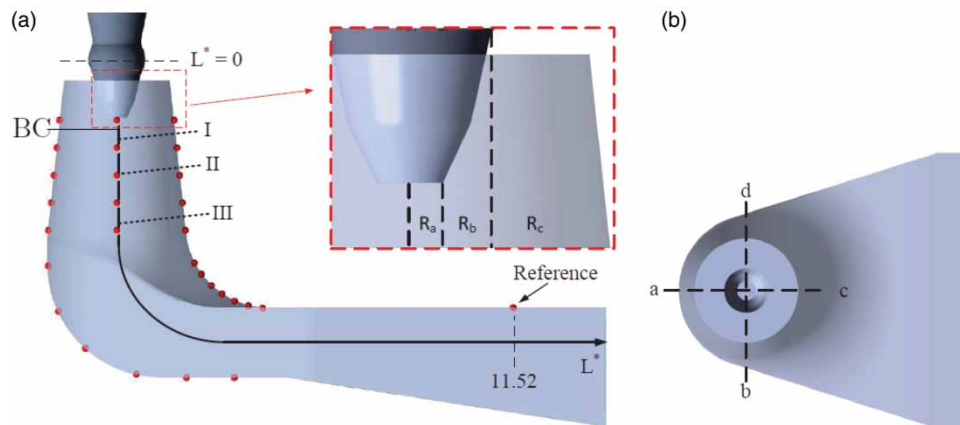

Figure 1. U9 draft tube with measurement locations. (a) The positions for the pressure taps are marked by red dots. In this paper, the pressure taps are numbered p1–p5 in the cone (starting from the top) and p6–p11 and p6–p12 along the outer and inner radius of the elbow, respectively. Sections I to III correspond to the LDA sections. (b) Circumferential positions for the pressure and LDA measurements in the draft tube cone.

Figure 2.   The computational domains, i.e., the guide vanes, the runner blades and the draft tube, and the boundary conditions.

the normalized center line used to express the positions of the measurements (Figure 1). The pressure measurements were performed by Jonsson et al. (2012).

4.   Numerics

In the current study, a transient rotor–stator simulation is performed with the entire turbine assembly (Figure 2). Such a configuration allows for capturing the effect of unsteadiness in the simulations and should be more accurate than previous stage simulations, which neglect the effect of unsteadiness.

4.1.   Flow solver

The commercial software ANSYS-CFX-13.0 was used in this study. All computations were performed using the high-resolution discretization scheme for the continuity equation and the advection term in the momentum equation. The high-resolution scheme has a blend factor that varies between second and first-order accuracy as a function of the variable gradients in the flow regions to avoid non-physical oscillations. First-order upwind scheme was used for the advection terms in the turbulence equations. Because, for some of the turbulence models (RNG $k - \varepsilon$ and SST-SAS) used, the solution did not converge properly with high resolution. Since the current work compares different turbulence models it was decided to use the same setup for all cases. The $k - \varepsilon$ model simulations were performed with the high resolution (bland factor $\beta = 0.75$) and first-order upwind schemes for the advection terms in the turbulence equations. However, any significant difference in the results was not observed. The transient term in the Navier-Stokes equations was solved using a second-order backward Euler scheme. This scheme is implicit and conservative in time and, therefore, does not require a Courant number stability limit. However, to achieve accurate resolution of the time behavior of the flow, and for numerical stability reasons as well, the time step needs to be small enough to resolve the relevant details. The time step was set to 0.0002 s,

which corresponds to approximately 1° of revolution of the runner, for a total simulation time of 10 s.

4.2.   Boundary conditions

In low-head hydraulic turbines, there is a strong interaction between the runner and the draft tube. It is necessary to introduce this interaction into the simulations to achieve accurate results. During the Turbine-99 workshop, Cervantes and Engström reported the importance of the runner cone region for the flow simulation in the draft tube (Cervantes et al., 2005). They also noted the importance of the runner cone in estimating the pressure recovery in the Kaplan elbow draft tube.

Generally, the entire turbine assembly should be used for the CFD simulation of the flow in water turbines. However, using the entire turbine assembly might require excessive computer resources and simulation time. Additionally, it is nearly impossible to generate one complete good-quality mesh for the entire turbine. The flow domain is usually divided into several flow domains that are connected through interface connections. As the flow in the distributor is accelerating and is well defined in a 345° wrap angle spiral casing, the guide vanes region represents a satisfactory inlet region. The flow domains used in the current investigation are presented in Figure 2.

There are three standard techniques to simulate rotor–stator: the frozen rotor, the stage interface and the rotor–stator interface. In this work, unsteady simulations are performed and a transient rotor–stator interface is used. The frozen rotor interface calculation is used to initialize the simulations performed with the rotor–stator interface because it is numerically robust and computationally inexpensive. Previously, Mulu et al. (2011) investigated the Porjus U9 draft tube with a stage interface. Because the circumferential effect of the quantities are filtered through the averaging process using a stage approach, the use of a single guide vane and runner blade flow channel was possible. This reduced the computational domain substantially. The authors noted that the stage interface approach gives a general understanding of the draft tube flow; however, this approach fails to accurately predict the effect of the blade wakes and the hub-blade clearance. Furthermore, the turbulence models predicted an early separation on the runner cone (Figure 9). The flow near the runner cone is equivalent to a bluff body flow. RANS prediction of such flow is limited as RANS describes flows in a statistical manner, i.e., quasi-periodic large scale and chaotic small scales features cannot be distinguished (Breuer, Jovicic, & Mazaev, 2003). Nevertheless, the different models used predict differently separation. Figure 3 presents the shroud-blade and hub-blade clearances for the chosen blade tilt angle. The shroud-blade clearance at the leading and trailing edge is 2.25 and 1.25 mm, respectively; the minimum is 0.3 mm at the middle of the blade. For the hub-blade clearance the minimum is 0 mm and the maximum is 3 mm.
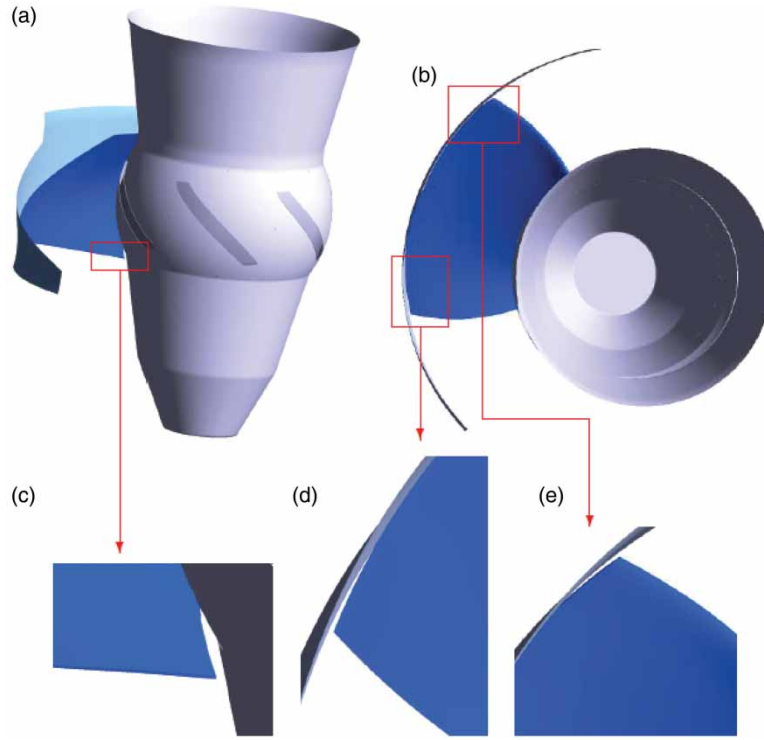
Figure 3. Shroud-blade and hub-blade clearances used in the simulation.

Fully conforming multiblock hexahedral meshes where generated for all components, including gaps in the runner part. A grid independence study was performed with steady state simulations to evaluate the effect of grid size on the solution. The pressure recovery

$$Cp_{cfd} = \frac{\frac{1}{A_{out}}\iint\limits_{A_{out}} PdA - \frac{1}{A_{in}}\iint\limits_{A_{in}} PdA}{\frac{1}{2}\rho\left(\frac{Q}{A_{in}}\right)^2} \quad (1)$$

And loss factor

$$\varsigma = \frac{\iint\limits_{A_{in}}\left(P+\rho\frac{|U|^2}{2}\right)U.\hat{n}dA - \iint\limits_{A_{out}}\left(P+\rho\frac{|U|^2}{2}\right)U.\hat{n}dA}{\left|\iint\limits_{A_{in}}\rho\left(\frac{|U|^2}{2}\right)U.\hat{n}dA\right|} \quad (2)$$

were the two quantities investigated because they are directly linked to the pressure and velocity variations in the flow domain. The performance of the draft tube is usually quantified with these two parameters as well when using CFD. The size of the three selected meshes and the value of the engineering quantities investigated are presented in Table1. In addition, the mean velocity profiles, at the location where the experimental measurements were performed, were compared for the three meshes and showed no significant differences. For the unsteady simulations the fine mesh was used.

The resolution of the stage interface was studied with the parameter "GGI stage groups max", which determines the smallest size for any given span range. Three different setups were used to study the sensitivity of the radial discretization: first without defining the "GGI stage groups max" parameter and then two values, 50 and 100, were used. When the parameter is set to a large number, the stage bands will be fine near the boundary layer regions where the mesh is very fine and denser where the mesh is coarser. However, in the current study varying this values shows no significant difference, therefore "GGI stage groups max" = 100 was used.

In the current study, the complete geometry of the guide vanes and the runner is used for the simulation together with the elbow draft tube. The three domains are connected to each other with a general grid interface. The mesh density used for the entire assembly is composed of approximately 17 million hexahedral cells. The draft tube mesh was generated with ICEM and the guide vane and the runner meshes were generated with ANDRITZ hydro/Poly

Table 1. Mean pressure recovery (Cpcfd) and loss factor (ζ) obtained from the three different mesh sizes.

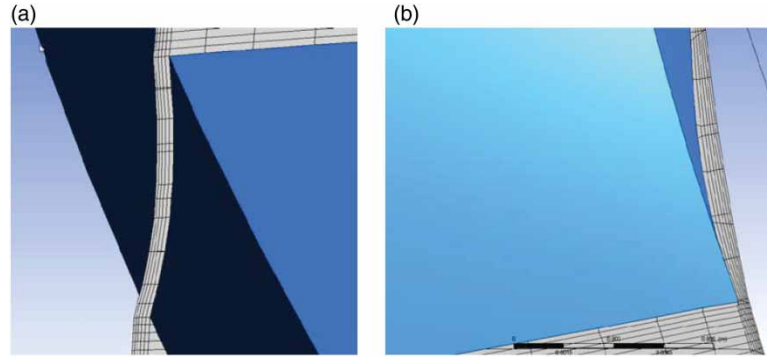| Grid size [millins]	17	8.9	3.9
Cp$_{cfd}$	0.90784	0.9078	0.9077
ζ	0.1403	0.1416	0.1433

Figure 4.   Mesh density at (a) the shroud and (b) the hub clearance, the number of cells in the clearance varies between 5 and 10.

Table 2.   Mesh properties used in the simulations.

	Cell	Face angle (min) [deg.]	Aspect ration	y+ (min/avg/max)
Guid vane	7485100	14	483	1.2/83.2/421.8
Runner	5926290	9	138	3.0/98.8/578.3
Draft tube	3700000	31	372	4.4/41.3/93.2

in-house code. In both methods an o-grid technique is used. Figure 4 presents the mesh resolution around the runner blades, hub and shroud. In the current study the number of cells used in the clearance at hub and shroud varied between 5 and 10. The mesh density and properties, such as the minimum angle, the aspect ratio and the y^+ values, are presented in Table 2. At the inlet, the mass flow rate with a flow direction is imposed. Previously, Mulu et al. (2011) performed a sensitivity study on the turbulence intensity for the draft tube and the stage simulations with different intensity values (1%, 5% and 10%). They found that the turbulence intensity did not play a significant role. Therefore, a turbulence intensity of 5% at the inlet was used in the current study. All walls were assumed to be smooth, and a no-slip wall condition was imposed for all solid surfaces. The wall velocity for the runner hub in the draft tube is set to 696.3 rpm. An angular velocity was imposed to the complete runner assuming no-slip boundary at the runner-fluid interface. At the outlet, an average static pressure over the entire outlet was specified to be 0 Pa. The transient solution at a given time step was considered converged when the value of the root mean square (RMS) residuals for each equation solved was less than 10^{-5}.

4.3.   Turbulence models

The governing equations are solved using the Reynolds average method and assuming an incompressible and isothermal fluid. This method is based on a statistical approach where time-averaging of variables is carried out to separate the mean from the fluctuations. The unsteady

Reynolds averaged Navier-Stokes continuity and momentum equations are given as:

$$\frac{\partial \bar{u}_i}{\partial x_i} = 0 \tag{3}$$

$$\frac{\partial \bar{u}_i}{\partial x_i} + \bar{u}_j \frac{\partial \bar{u}_i}{\partial x_j} = -\frac{1}{\rho}\frac{\partial \bar{p}}{\partial x_i} + v\frac{\partial^2 \bar{u}_i}{\partial x_i^2} - \frac{\partial \overline{(u_i' u_j')}}{\partial x_j} \tag{4}$$

where $\overline{u_i'}$ are the time-averaged velocity components, $\bar{p}$ is the time-averaged pressure, ρ is the fluid density, v is the fluid kinematic viscosity, t is the time and u are the fluctuating velocity components.

As a result of the Reynolds averaging, in Equation (4), there is an additional stress term acting on the mean flow due to the fluctuating velocity, which is known as the Reynolds stress ($\tau_{ij} = -\overline{u_i' u_j'}$). This term represents the effect of the turbulence on the mean flow. The Reynolds stress term introduces six unknown variables in the governing equations, which must be modeled. Generally, the RANS turbulence models can be broadly divided into two types: eddy-viscosity models and Reynolds stress models. The eddy-viscosity models are based on the Boussinesq hypothesis, which relates the Reynolds stresses to the mean velocity gradients via the eddy viscosity:

$$\tau_{ij} = -\overline{u_i' u_j'} = v_t\left(\frac{\partial \bar{u}_i}{\partial x_j} + \frac{\partial \bar{u}_j}{\partial x_i}\right) - \frac{2}{3}\left(k + v_t\frac{\partial \bar{u}_k}{\partial x_k}\right)\delta_{ij} \tag{5}$$

where $k = \frac{1}{2}(\overline{u_i' u_j'})$ is the turbulent kinetic energy, δ_{ij} is the Kronecker delta, and v_t is the turbulent viscosity (also known as the eddy viscosity) and has to be modeled. In the two-equation eddy-viscosity models, the turbulent properties of the flow are represented with the inclusion of two extra transport equations: one equation for the turbulent kinetic energy, k, and one equation for the turbulent dissipation rate, ε, or the specific dissipation rate, ω. This means that both the velocity and turbulent length scale are solved using separate transport equations.

The flow prediction in the runner and draft tube is very sensitive to the boundary conditions applied and the turbulence model selected (Cervantes, 2003; Menter, 2003).

In this situation, the flow exhibits characteristics (e.g., streamline curvature) that are outside the scope of the experiments for which the turbulence models have been calibrated (Menter, 2003). Different two-equation RANS models were used in the present work to evaluate their capability to reproduce the flow in a Kaplan turbine at the BEP (k − ε, RNG k − ε and SST) and the scale adapted simulation (SAS) model.

In the standard k − ε model, the eddy viscosity is related to the turbulent kinetic energy and the dissipation rate using the following assumption: $\nu_t = C_\mu \frac{k^2}{\varepsilon}$, where C_μ is a model constant (Durbin & Reif, 2001). The standard k − ε model has proven to be robust and relatively accurate for a large number of engineering flows and is widely used in industry because it can be solved relatively fast compared with other turbulence models. However, this model performs poorly for complex flows involving a large adverse pressure gradient, separation, rotation, and a strong streamline curvature. Another major drawback associated with this model is the over prediction of the eddy viscosity near the wall; thus, this model requires special treatment at the wall (Durbin & Reif, 2001; Pope, 2000; Wilcox, 1993). In the present study, scalable wall functions (see Vieser, Esch, & Menter, 2002) were used with the k − ε model. Wall functions allow not resolving the flow near the wall. It assumes that mesh points near the wall lie in the logarithmic region of the boundary layer, thereby allowing modeling the wall shear-stress using a logarithmic profile assumption. In cases where points are very close to the wall, the logarithmic assumption does not hold, and a limit on the minimum acceptable y_+ is automatically imposed in the computation of the wall shear-stress, making the wall function scalable.

The RNG k − ε model is based on the renormalization group analysis of the Navier-Stokes equations and attempts to overcome some of the limitations of the standard k − ε model. The transport equation for the turbulent kinetic energy is the same as the equation in the standard k − ε model. The major difference between these models is that the model constants of the transport equations for the dissipation rate vary. Additionally, the constant coefficient related to the turbulence production term due to the viscous forces is replaced by a function in the case of the RNG model. This function includes the effect of rapid strain and the streamline curvatures. The RNG model also includes the effect of the swirl on the turbulence, which enhances the accuracy for swirling flows (Wilcox, 1993). Furthermore, the RNG model takes into account the different turbulent length scales (Yakhot, Orszag, Thangam, Gatski, & Speziale, 1992). Scalable wall functions were also used with this turbulence model.

In the near-wall boundary layer, the Wilcox model (k − ω) is more accurate than k − ε. However, the Wilcox model has the disadvantage of a strong sensitivity to the value of ω in the free stream outside the boundary layer (Menter, 1992; Wilcox, 1993). This problem can be overcome by combining the k − ω in the near-wall region with the free stream independence of the k − ε model far from the wall, which is the base for the zonal shear stress transport (SST) model. In the SST model, blending functions are used to ensure a proper selection of k − ε and k − ω zones. The main advantage of the SST model is its ability to accurately predict the onset and the amount of flow separation under high adverse pressure gradients. This is because the model accounts for the transport effects of the turbulent shear stress (Menter, 1994). Bardina, Huang, and Coakley (1997) have shown the ability of the SST model to predict separation in an adverse pressure gradient. The results obtained by Marjavaara et al. (2005) also confirm the ability of the SST model to perform well in a Kaplan draft tube.

The SST-SAS turbulence model is used for transient cases. The SST-SAS model differs from the URANS SST model by adding an additional scale adapted source term (SAS) in the ω transport equation. The SST-SAS model uses the von Karman length scale for the turbulence scale equation to detect the unsteadiness. For flows with transient behavior, the SAS model dynamically adjusts to resolve the turbulent structures based on the information provided by the von Karman length scale and results in a LES-like behavior in unsteady regions of the flow field. The model provides the standard RANS model in stable flow regions. More details about the SST-SAS model can be found in Egorov, Menter, Lechner, and Cokljat (2010).

The Reynolds stress models solve the transport equations for each Reynolds stress and for the ε or ω that provide the length and time scales of the turbulence (Pope, 2000). The isotropic eddy-viscosity hypothesis is avoided. However, some terms must still be modeled, such as the pressure-strain, the dissipation rate, and the turbulent diffusion. The RSM models have the potential to accurately predict complex flows because they account for the effects of streamline curvature, swirl, rapid changes in the strain rate and anisotropy of the turbulent stress. A drawback of the model is that it demands more computer resources because more equations are solved, and the model is less robust than the linear eddy-viscosity models. Mulu et al. (2011) show that the RSM model performs well in a draft tube simulation without including the upstream geometry. However, in the current study, it was very difficult to achieve convergence using the RSM model. A very small time step was necessary to avoid divergence, and made the simulation convergence impossible in a reasonable period of time, i.e., less than one week using 100 cores.

5. Engineering quantities

There is significant quantity of kinetic energy leaving the runner in reaction turbines, especially in low head turbines. The amount of kinetic energy that is converted to pressure energy at the runner exit defines the performance of the draft tube. The pressure recovery factor, Cp, is a common

engineering quantity used to quantify the amount of kinetic energy recovered along the draft tube. Cp is defined as the ratio of the pressure difference at the outlet and inlet of the draft tube to the dynamic pressure of the mean axial velocity at the inlet. In the current study, the performance of the draft tube was quantified by calculating the pressure recovery factor based on the wall pressure (Equation 6) (Gubin, 1973), because this value is experimentally available from Mulu et al. (2012).

$$Cp_w = \frac{P_{wall} - P_{wall\_inlet}}{\frac{\rho}{2}\left(\frac{Q}{A_{inlet}}\right)^2} \tag{6}$$

where P_{wall_inlet} and A_{inlet} are the static wall pressure and the cross-sectional area at position p1 in the cone, P_{wall} is the static wall pressure along the draft tube and Q is the flow rate (Figure 1).

The wall pressure recovery is an estimation of draft tube efficiency because it only considers the wall pressure rather than the average pressure across the whole cross section, thus it doesn't take into account the pressure variation in the radial direction. Cp_w is also based on the average kinetic energy at the inlet, which means that the swirling motion and non-uniform velocity profiles effects are neglected. Experimentally, it is difficult to obtain the average pressure over the cross-section along the radius, therefore, Cp_w is a common parameter used to characterize draft tubes.

At the runner exit there is a residual swirl, depending on the operating conditions and the runner type. Some swirl may be advantageous in the conical diffuser. Swirl can also cause instability that leads to vibration, noise, fatigue failures, power swings, vertical movements of the turbine, and reversed flow at the centre of the draft tube. Hydraulic turbines are usually designed to have an optimal swirl at the exit of the runner when operating at the BEP, which allows high pressure recovery and no flow separation at the draft tube cone wall (Gubin, 1973). The intensity of the swirl is characterized by the swirl number, which is determined by the ratio of the axial flux of the angular momentum to the axial momentum flux times the equivalent radius, as shown in Equation 7 (Senoo & Nagata, 1972).

$$S_w = \frac{\int_0^R UVr^2 dr}{R\int_0^R U^2 r dr} \tag{7}$$

where U is the axial velocity component, V is the tangential velocity component and R is the equivalent exit radius.

6. Data reduction

The experimental velocity measurements were performed using a laser Doppler anemometry (LDA) technique. The data was collected at several points along the radius because LDA is a point-wise measurement method. The time-averaged profile was obtained after several rotations of the runner at a fixed radial position. The phase-resolved velocities were obtained by decomposing the instantaneous velocity with a Reynolds triple decomposition method,

$$u(x,t) = \bar{u}(x) + \tilde{u}(x,t) + u'(x,t) \tag{8}$$

where $u(x,t) = \langle u(x,t)\rangle + u'(x,t)$ is the instantaneous quantity, $\bar{u}(x,t)$ is the time-averaged quantity, $\tilde{u}(x,t)$ is the periodic fluctuation quantity and $u'(x,t)$ is the random fluctuation quantity. $\langle u(x,t)\rangle$ is the phase-averaged quantity over the cycles. The velocity measurements were related to the runner angular position using an encoder signal. A circumferential resolution of 3° was used to calculate the time-averaged velocity data. A detailed description of the method can be found in Mulu et al. (2012).

In the case of the CFD, the velocity and pressure information were obtained at every time step for a complete rotation of the runner. The simulation time step corresponds to approximately 1° of runner rotation. The time-averaged velocities in the simulation were obtained in a similar fashion as in the experiments, i.e., the velocity information at a fixed radial position was used to calculate the averaged and angular velocities. Because the experimental values are obtained with a circumferential resolution of 3°, the simulation results are also phase-resolved with the same circumferential resolution. The experimental axial velocity obtained at sections I-III is slightly different from the true axial velocity because the LDA probe was orthogonal to the draft tube cone wall. The same component was extracted from the simulations and is presented in various figures.

For the CFD calculations, the wall pressures are extracted over a period at the same point where the experimental measurements were performed (Figure 1).

7. Results and discussions

The simulated time-averaged and phase-resolved pressures and velocities are presented and compared to the experimental results at different locations in the draft tube. The time-averaged and phase-resolved velocities are non-dimensionalized using the bulk velocity obtained from the flow rate and the area at section I, unless otherwise mentioned. The measured radii are non-dimensionalized with respect to the runner radius. The positive directions for the axial velocity and tangential velocity are defined vertically down through the draft tube cone and clockwise from the top of the runner, respectively.

7.1. Engineering quantities

Figure 5 presents the wall pressure recovery of the conical diffuser obtained experimentally and numerically using four different turbulence models at four angular positions (Figure 1). The wall pressure recovery is defined
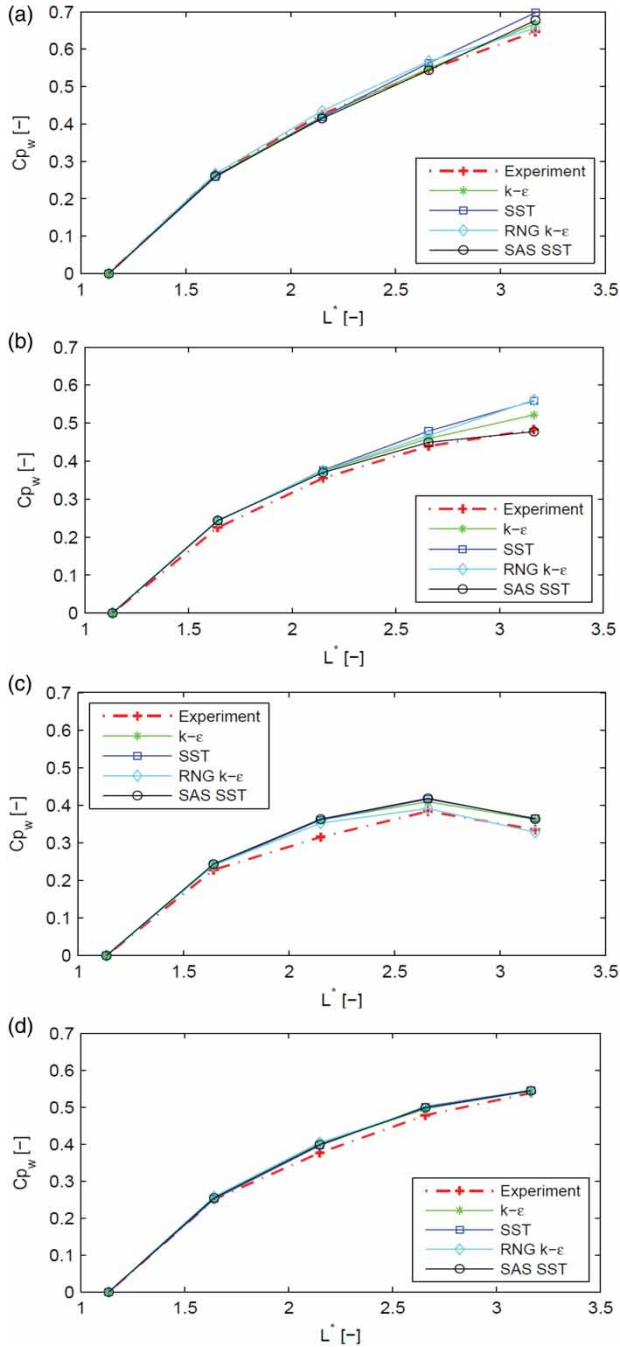
Figure 5. Wall pressure recovery, Cp_w, of the draft tube cone obtained from experimental measurements and CFD calculations (a) Angular position a. (b) Angular position b. (c) Angular position c. (d) Angular position d (Figure 1). L* is the normalized centerline of the draft tube.

by Equation 6. The pressure recovery factor indicates the degree of conversion of the kinetic energy into static pressure, and a higher value indicates a higher efficiency of the region considered. Both the experimental and the numerical pressure recovery Cp_w increase in the downstream direction, which indicate the correct operation of the draft tube cone. The numerical results show similar values of Cp_w at all angular positions compared with the

experimental results. From both the experiments and the simulations, the highest pressure recovery is obtained at section a, specifically at the end of the conical diffuser (Figure 5a). This is expected because the flow decelerates towards the outer radius of the elbow, and thus, the static pressure increases. At section c, the recovery is low due to the acceleration of the flow toward the inner radius of the elbow and, as a result, the static pressure decreases (Figure 5c).

The wall pressure recovery is well predicted with all turbulence models in this part of the draft tube. The largest discrepancies between the experimental and the numerical results occur at section b (Figure 5b). At approximately L* = 3.2, the wall pressure recovery is overestimated in the simulations, except when using the SAS model, compared with the experiment.

Figure 6 shows the wall pressure recovery Cp_w along the upper and lower paths in the draft tube for the four turbulence models together with the experimental results. The results from both the experiments and the simulations show that Cp_w along the upper path is low at the beginning of the inner radius of the elbow because the flow accelerates in that area. Then, the pressure recovery increases along the radius from L* = 4 to L* = 7 (Figure 6b). Conversely, Cp_w along the lower path continues increasing up to L* = 5 and starts to decrease along the elbow radius. In the elbow of the draft tube, all turbulence models predict the same behavior as the experiments with slight differences between each model. These differences may be attributed to how each turbulence model handles the strong streamline curvatures.

Figures 5 and 6 indicate that most of the pressure recovery occurs in the conical diffuser in both the experiments and the simulations. From the results presented, all the investigated turbulence models did not experience any difficulty predicting the pressure distribution along the draft tube.

Figure 7 presents the flux of angular momentum ($FAM = \int_0^R UVr^2 dr$) obtained from the experiments and the RNG $k - \varepsilon$ turbulence model. The results from the other turbulence models are similar to that of the RNG $k - \varepsilon$ model; therefore, the results are not presented here. The flux of angular momentum increases from the centre to the draft tube cone wall in both the experimental and the simulation results. The flux of the angular momentum is conserved, i.e., the tangential velocity is nearly unaltered by the diffuser, cf. Figure 8. The experimental and the numerical results are similar from the centre until r' = 0.75. However, there is a difference close to the draft tube cone wall.

Swirl plays a vital role in the transformation of kinetic energy into pressure energy in the draft tube cone, because it can prevent flow separation at the cone wall. The swirl numbers calculated, using Equation 7, from the experiments and the simulations are presented in Table 3. The swirl numbers obtained from each turbulence model at
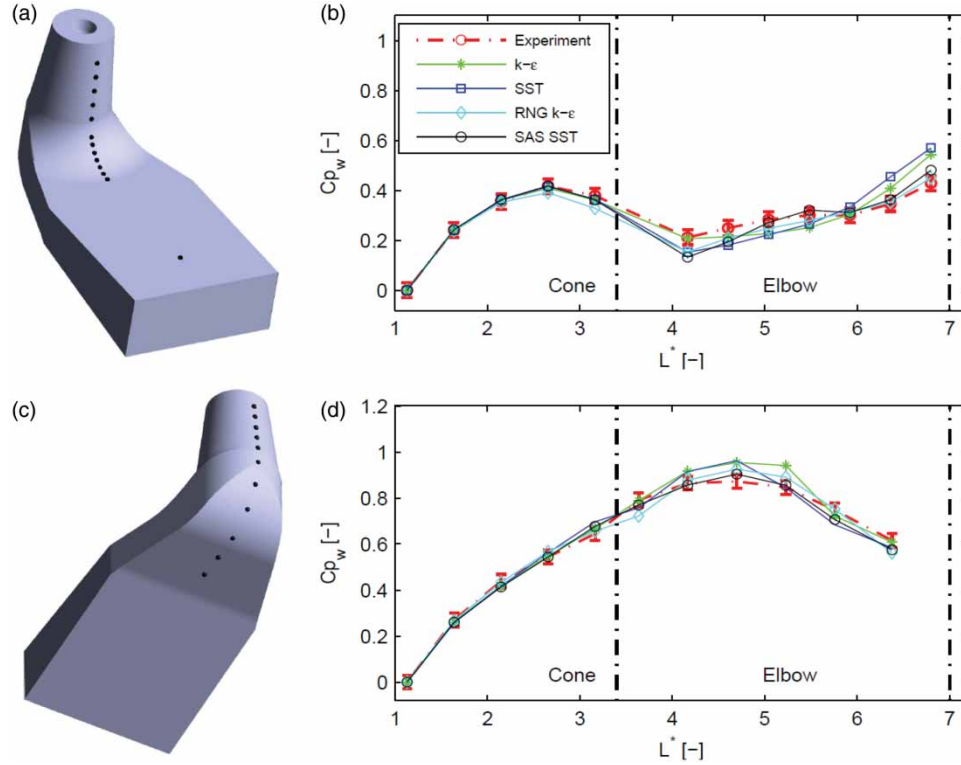
Figure 6. (a) Positions along the upper sensor path in the draft tube cone and elbow. (b) Wall pressure recovery along the upper path. (c) Positions along the lower sensor path in the draft tube cone and elbow. (d) Wall pressure recovery along the lower path. L* is the normalized centerline of the draft tube.
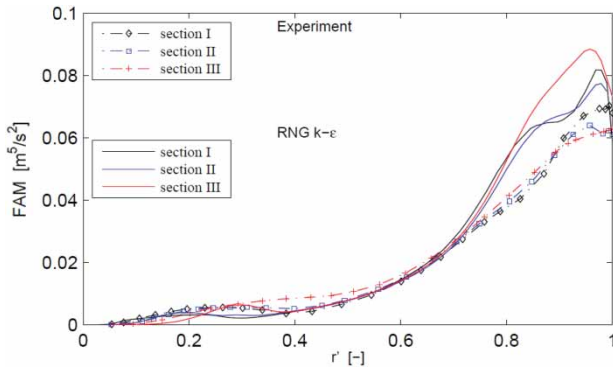

Figure 7. Experimental and numerical (RNG $k - \varepsilon$ model) angular momentum flux at sections Id, IId, and IIId. The radius is normalized by the radius at each section.

each measurement section are approximately equal to the experimental values. However, there are small differences between the results of the different turbulence models. The $k - \varepsilon$ model seems to predict the swirl number best.

7.2.   *Time averaged quantities*

The time-averaged velocity profiles obtained using the unsteady state computations are compared to the experimental data at three different sections (I, II, and III) in the draft tube cone below the runner hub.

As shown in Figure 8, the results from the four turbulence models ($k - \varepsilon$, RNG $k - \varepsilon$, SST and SAS-SST) are compared with the experimental data. The CFD results fit well with the measurement in the region R_c for all turbulence models used. This region corresponds to the blade wake (hub-shroud) where the effects of the viscosity are negligible. Some difference appears between the experimental and the numerical results of the axial velocity near the wall at section I, especially for the RNG and $k - \varepsilon$ models. Flow at the draft tube wall is sensitive to the tip vortex developing at the blade-shroud clearance (Breuer et al., 2003). The bump at $r^* = 0.9$ is characteristic. The axial velocity is somehow overestimated in measurement section III. The major differences appear in the regions R_a and R_b for the axial and tangential velocity at section I, II and III. In measurement sections I and II, the $k - \varepsilon$ and RNG $k - \varepsilon$ models overestimate the axial and tangential velocity components in region R_a, whereas the SST and SAS-SST models underestimate these velocities. In section III, all turbulence models underestimate the axial and tangential velocities.

For this application, the unsteady computation yields a significant improvement over the steady state stage computation, especially in section I, as shown in Figure 9 (Mulu et al., 2011). In the previous stage simulations, the computational flow domain comprised a single guide vane and runner blade flow channel together with the draft tube.
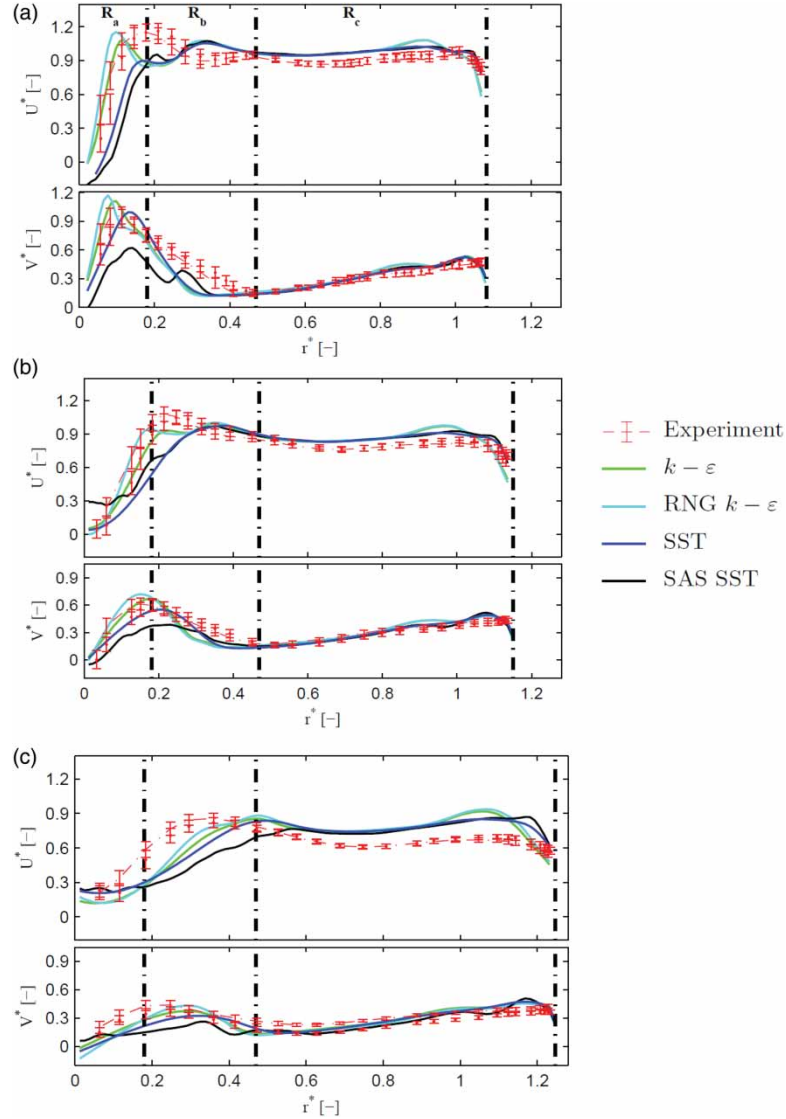
Figure 8.   Experimental and simulated mean axial (U*) and tangential (V*) velocities (a) Section I, (b) Section II and (c) Section III. The experimental results are presented with bars representing the velocity fluctuations at angular position d.

Table 3.   Experimental and numerical swirl numbers.

Sw	Id	IId	IIId
Experiment	0.255	0.277	0.332
k − ε	0.255	0.277	0.316
RNG k − ε	0.254	0.272	0.294
SST	0.253	0.273	0.231
SAS SST	0.250	0.271	0.300

However, in the present transient rotor–stator simulation, the entire turbine flow domain was used. The simulation results obtained with the $k - \varepsilon$ model are similar to that of the RNG $k - \varepsilon$ model; therefore, only the $k - \varepsilon$ results are presented.

In the stage computation, the flow recirculation occurs early in the hub region, which explains why the axial and tangential components are underestimated in the R_a and R_b regions for sections I, II, and III. In both Figures 8 and 9 there is a difference between the experimental and numerical results between R_a and R_b. For the stage simulation due to the early separation the maximum velocity is observed in R_b. During the transient rotor–stator simulation, there is no early separation. The velocity between R_a and R_b decreases and then increases in R_a. This behavior is attributed to the wakes created by the jets and blade channels interaction where the velocity decreases within the wakes.

The draft tube entrance is a double diffuser; the area increases outwards and inwards. In order to ensure an attached flow to the draft tube cone wall, some swirl must still be present in the flow leaving the runner. To keep the flow attached to the runner cone, the required conditions are different. The runner cone rotates faster than the fluid and thus increases the angular momentum of the fluid leaving the runner. The condition is not appropriate
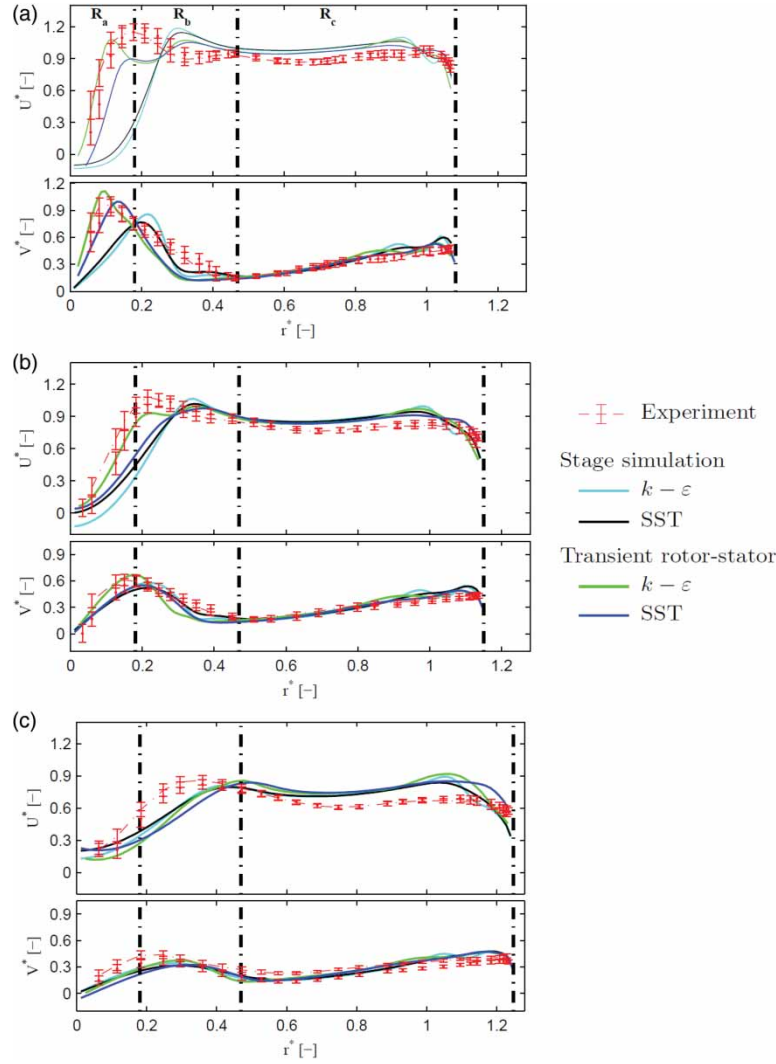
Figure 9.   Experimental and simulated mean axial (U*) and tangential (V*) velocities (a) Section I, (b) Section II and (c) Section III. The experimental results are presented with bars representing the velocity fluctuations at angular position d. The stage simulations were performed with one guide vane flow channel, one runner blade flow channel and the draft tube. The transient rotor-stator simulations were performed with the entire turbine assembly, i.e., twenty guide vanes, six runner blades and the draft tube. A detailed description of the stage simulation can be found in Mulu et al. (2011).
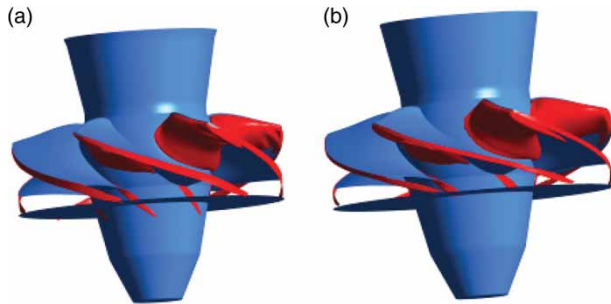
Figure 10.   Isosurface of the axial velocity in the stationary frame (U = 6.5 m/s) in the runner and draft tube regions. The disk below the runner blades represents the interface between the regions. (a) unsteady results of the complete rotor–stator simulations and (b) results of the stage simulation.

to keep the flow attached to the runner cone. To avoid separation, the boundary layer needs to be energized; this is done with a special clearance on the blade allowing the

formation of a jet in the runner cone boundary layer, see Figure 10a.

The stage calculation averages the flow velocity upstream the interface. The jet thus disappears from the calculation at the runner–runner cone junction, see Figure 10b. The jet absence promotes early separation on the runner cone explaining the main difference between the transient and stage simulations.

Figure 11 shows a comparison of the computed and measured mean flow angle at section Id, IId, and IIId. The experimental flow angle is compared with those obtained with the $k - \varepsilon$, the RNG $k - \varepsilon$ and the SST model. All turbulence models demonstrate similar results except the SST model in region R_a at section IIId. The numerical simulations are unable to capture the correct angle towards the end of the draft tube cone. The main reason is an underestimation of the axial velocity in the vortex core leading to an over-estimation of the axial velocity in region R_c.
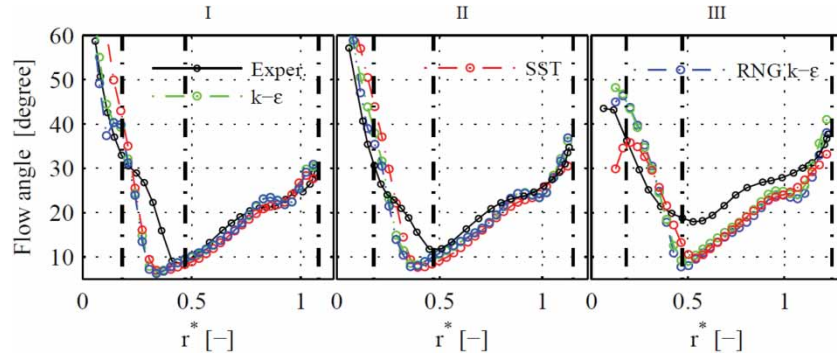
Figure 11.   Flow angle, i.e., arctan (V/U), at sections $Id - IIId$, from the experiment and the simulations.
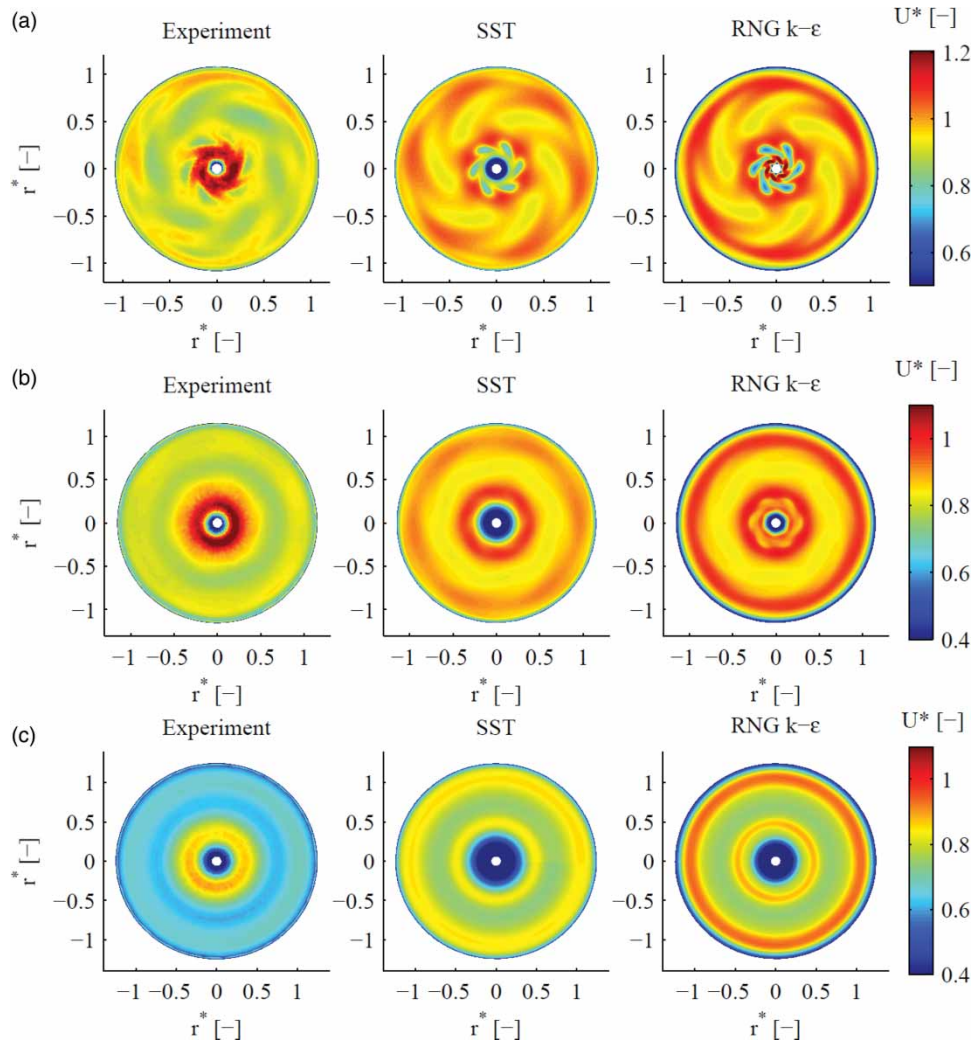

Figure 12.   Phase-resolved axial velocity for one runner revolution. (a) Section Id (b) Section IId and (c) Section IIId.

7.3.   *Phase-averaged quantities*

The experimental and numerical results of the phase-resolved axial and tangential velocities are presented in Figures 12 and 13, respectively. The results of two turbulence models, SST and RNG $k - \varepsilon$, are presented since they are representative of the results obtained using the other turbulence models.

In Figure 12, the blade wakes, which are low axial velocity regions, are clearly discernible at section I for both the experiments and the simulations. The blade wakes signatures are, however, more pronounced in the simulations than in the experiments, where they are smeared out and join each other. The velocity is slightly lower below the blades in the experiments compared with the simulations,
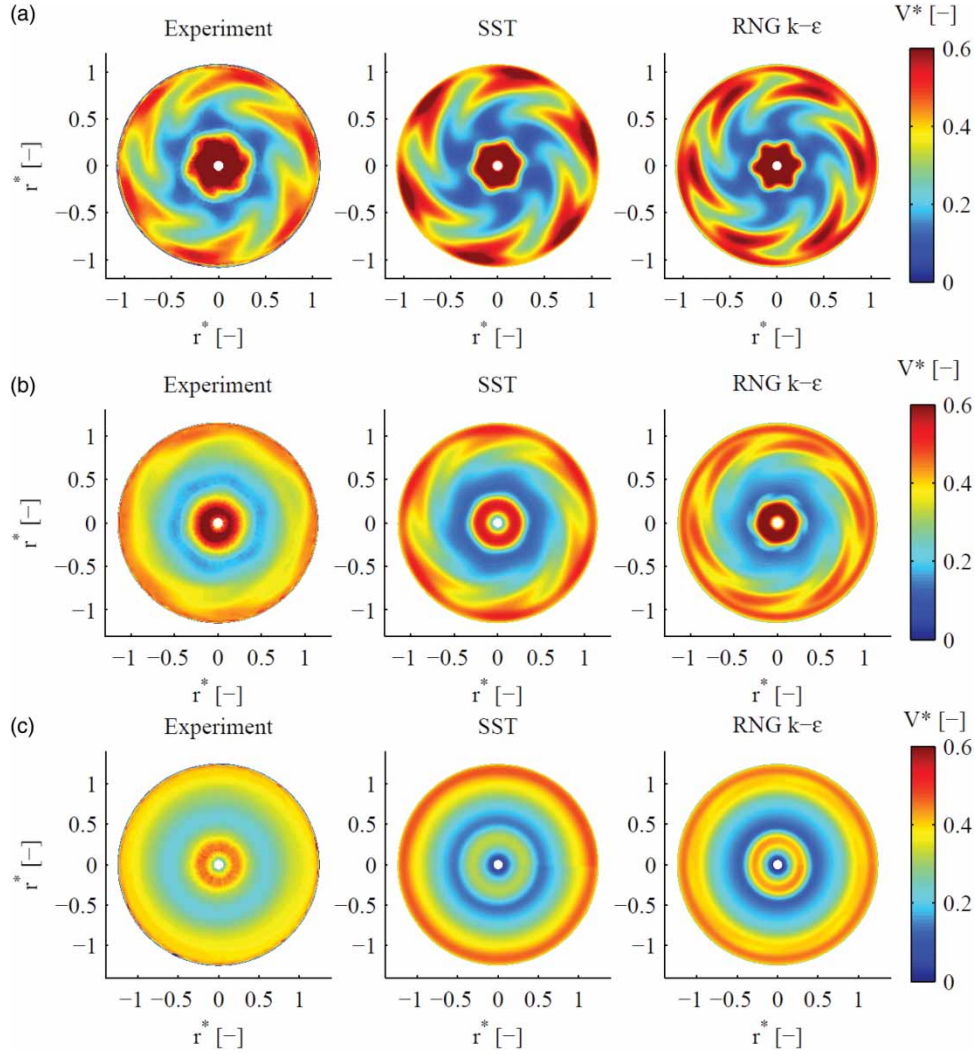
Figure 13.   Phase-resolved tangential velocity for one runner revolution. (a) Section Id (b) Section IId and (c) Section IIId.

because higher velocities are obtained below the runner cone. The main difference between the SST and the RNG k − ε turbulence models is found below the runner cone.

The small wakes that were counter rotating below the runner cone due to the blade-hub clearances, i.e., due to the flow jet coming out of the blade-hub clearances with high velocity, are also captured in the simulations, see Figure 14. However, the large axial velocity beneath the runner cone is not captured by any turbulence model. The reason is attributed to the inability of the turbulence models to predict flows with a strong streamline curvature (Menter, 2003). Figure 14 presents the swirling strength of the vortex core region which represents the strength of the local swirling motion. The main flow domain rotates clockwise except for the portion of the flow leaving through the blade-hub clearance, where the swirling strength shows counter-clockwise vortices.

At section II and III, the blade wakes have disappeared in both the experiments and the simulations. The results are
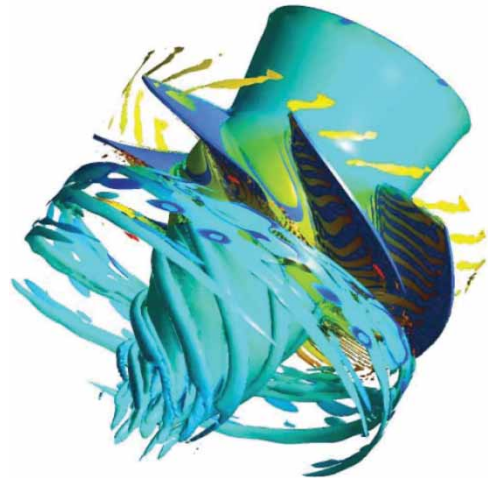

Figure 14.   Swirling strength of the vortex core region.

now similar to the mean results presented in Figure 8. The Figures point out an overestimation of the velocity below the blades and an underestimation below the runner cone
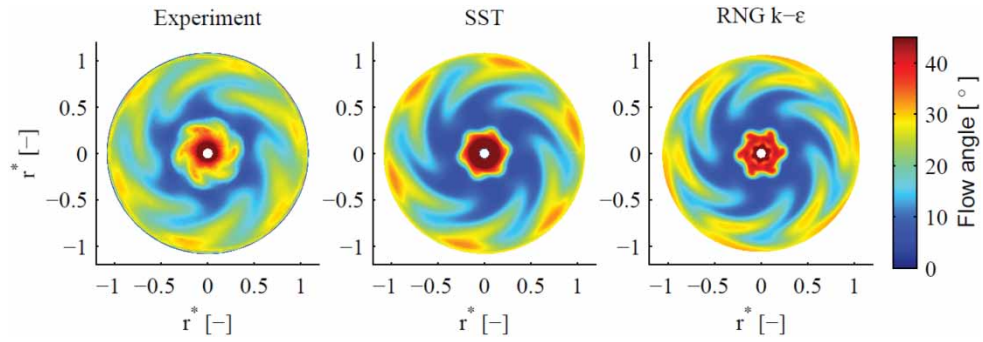
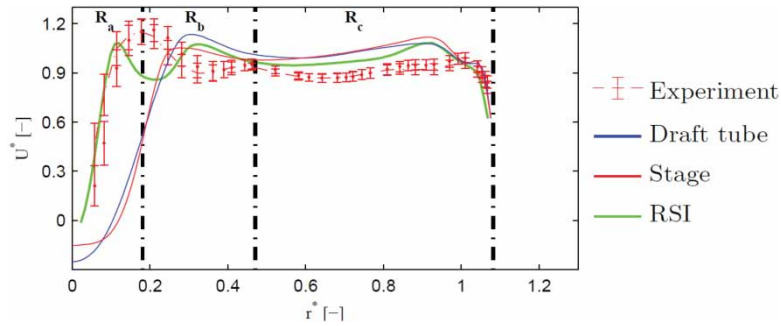Figure 15.   Phase-resolved flow angle at section Id for one runner revolution.

Figure 16.   Axial velocity profile at section Ia; experimental and numerical results with $k - \varepsilon$.
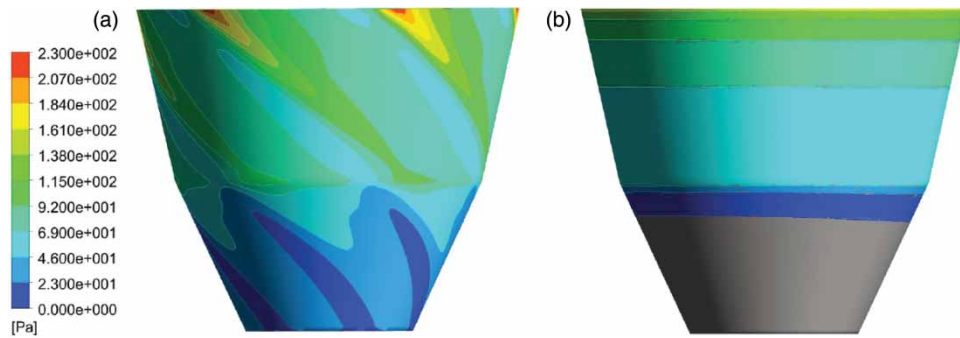

Figure 17.   Axial wall-shear stress on the runner cone for the (a) RSI and (b) draft tube simulations with $k - \varepsilon$. The grey color indicates a negative wall shear stress, i.e., separation on the runner cone.
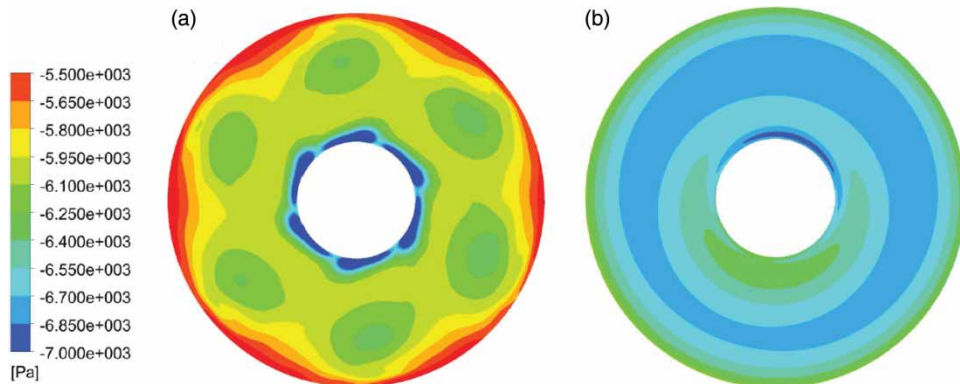

Figure 18.   Pressure on a plane normal to the runner cone for the (a) RSI and (b) draft tube simulations. The plane is situated just below the circle delimiting the runner cone in 2 regions, see Figure 17.

compare to the experimental results. The results are similar for both turbulence models.

The phase-resolved tangential velocity results obtained from the simulations are in better agreement with the experiments than for the axial velocity (Figure 13). The blade wakes are represented by high velocity, dark red regions. The amplitudes are similar, independent of the turbulence model used with few noticeable differences. The blade velocity deficit, which is the dark blue regions, near the hub is larger in the simulations. Furthermore, the higher tangential velocity spots are the blade trailing edges near the draft tube cone, which are difficult to discern in the experiments. This difference may be attributed to an insufficient number of samples in each bin in the experiment, which may affect the phase value.

At section II, the blade wakes are still present in the simulations and are function of the turbulence model used. Furthermore, the amplitude of the tangential velocity at section II is higher in the simulations, similarly to section III, where all wakes have disappeared.

The phase-resolved flow angle at section I is presented in Figure 15. The results at the other two sections are not presented because they are similar to the graph presented in Figure 11. The lower flow angles, blue region, are found between the blade wakes where the flow is nearly axial. In the blade wake regions, high shear induces large tangential velocity and flow angles. These three figures are found to be similar with a smaller angle in the inter-blade wakes for the simulation.

In order to quantify the effect of the jets, the velocity and turbulent quantities were extracted from the transient simulations (RSI) at the runner-draft tube interface. Numerical simulation of the draft tube alone was performed with the circumferentially averaged quantities from the transient simulations as inlet boundary conditions. The axial velocity profiles at section Ia for the RSI, stage and draft tube simulations are presented in Figure 16. The stage and draft tube simulation results similarly point out the specific effect of the jets. An early separation appears on the runner cone without the jets. The circumferential distribution of the energy affects the flow near the runner cone.

The axial wall-shear stress on the runner cone is presented in Figure 17 for the RSI and the draft tube. The effect of the jets is significant on the runner cone. Higher wall-shear stress is obtained locally. The flow is completely attached until the end of the runner cone for the RSI case. The gray color on the runner cone of the draft tube simulations signifies a negative wall-shear stress, i.e., separation.

The pressure on a plane normal to the runner-cone is presented in Figure 18 to illustrate better the phenomenon. The high-velocity jets near the runner cone create a lower pressure region for the RSI simulation, see the dark blue region. The lower pressure allows bending the streamlines toward the runner-cone, avoiding separation on the runner cone despite the centrifugal force imposed to the fluid. The pressure contour plot for the draft tube simulation is different. Lower gradient is captured in the pressure variation due to the circumferential averaging of the inlet quantities. Furthermore, a high pressure region near the runner cone is captured leading to an earlier separation.

8. Conclusion

URANS simulations of a Kaplan model were performed at the BEP. The numerical domain comprised the guide vanes, the runner and the draft tube and was discretized with a high-density mesh. The simulations were performed for four different turbulence models: $k - \varepsilon$, RNG $k - \varepsilon$, SST and SAS SST.

A comparison of the engineering quantities, the mean velocity profiles and the phase-resolved velocities obtained from the simulations with the experimental results show the ability of such simulations to capture the main draft tube flow characteristics. A good agreement was globally obtained independently of the turbulence model used. The methodology used, transient rotor–stator simulation, is a step forward compared to previously presented stage simulations.

The numerical wall pressure results presented the best agreement with the experiments. Some discrepancies appeared at the draft tube elbow inlet.

The numerical mean velocity profiles are similar in the blade wake region. The numerical results slightly overestimate the axial velocity, while the tangential velocity is well predicted and matched the experimental results. The main discrepancies appear below the runner cone. The experimental bump in the axial velocity is not captured by any turbulence model. The $k - \varepsilon$ and RNG $k - \varepsilon$ models best fit the results, while the SST and SAS SST models clearly underestimate the axial velocity. Further down the draft tube, the discrepancy between the experiments and the numerical results is amplified. The discrepancy may be attributed to the difficulty in predicting flows with strong streamline curvature for the turbulence models used.

The blade wake signatures are clearly visible in the numerical phase-resolved axial velocity at the inlet of the conical diffuser. These wakes are mixed and dissipated further downstream, as in the experimental results. The blade wake signatures are more pronounced for the simulations than for the experiments. Beneath the runner cone, the main effect of the blade-hub clearance is captured by the simulations. However, all turbulence models have difficulties predicting the high axial velocity region produced by the blade-hub clearance to ensure an attached flow to the runner cone. Independently of the turbulence model used, the phase-resolved tangential velocity results are in better agreement with the experiments when compared with the axial velocity. The hub clearance plays an important role in Kaplan draft tube flow. Accurate simulation

of this region is necessary to obtain physically representative results. A mesh sensitivity analysis with various turbulence models is necessary to quantify the exact contribution of the hub clearance modeling to the final numerical results.

The turbulence models are able to predict the behaviour of the free and forced vortexes with the exception of the SAS SST model. The k − ε and RNG k − ε models underestimate the effects of blade tip clearances, while the SST model captures this effect much better. The reason for this is attributed to its ability to perform better under a strong adverse pressure gradient. Even if the RNG k − ε model accounts for the effect of the rapid strain, the strong streamline curvature and the swirling motion (vorticity), the numerical results demonstrated no significant gain over the k − ε model. The SAS SST model performed poorly in predicting the phase-resolved velocity compared with the other models. The blade-shroud clearance seems sensitive to the turbulence model used. As draft tube flows are sensitive to initial boundary layer, this issue should be further analyzed.

References

Bardina, J. E., Huang, P. G., & Coakley, T. J. (1997). *Turbulence modelling validation testing and development* (Technical memorandum). NASA.

Breuer, M., Jovicic, N., & Mazaev, K. (2003). Comparison of DES, RANS and LES for the separated flow around a flat at plate at high incidence. *International Journal for Numerical Methods in Fluids, 41*, 357–388.

Cervantes, M. J. (2003). *Effects of boundary conditions and unsteadiness on draft tube flow* (PhD thesis). Sweden: Lulea University of Technology.

Cervantes, M. J., Engström, T. F., & Gustavsson, L. H. (Eds.). (2005). *Proceedings of Turbine-99 III: 3rd IAHR/ERCOFTAC Workshop on Draft Tube Flow*. Luleå, Sweden: Luleå University of Technology.

Ciocan, G. D., Iliescu, M. S., Vu, T. C., Nennemann, B., & Avellan, F. (2007). Experimental study and numerical simulation of the FLINDT draft tube rotating vortex. *Journal of Fluids Engineering, 129*(2), 146–158.

Duprat, C., Balarac, G., Metais, O., Tridon, S., Barre, S., Ciocan, G. D., Laverne, T., & Tomas, L. (2009). *Large-eddy simulation of draft tube flow and validation from experimental measurements*. 3rd IAHR International Meeting of the Workgroup on Cavitation and Dynamic Problems in Hydraulic Machinery and Systems.

Durbin, P. A., & Reif, B. A. P. (2001). *Statistical theory and modeling for turbulent flows*. Chichester: John Wiley.

Egorov, Y., Menter, F. R., Lechner, R., & Cokljat, D. (2010). The scale-adaptive simulation method for unsteady turbulent flow predictions. part 2: application to complex flows. *Flow Turbulence and Combustion, 85*, 139–165.

Gagnon, J. M., Aeschlimann, V., Houde, S. B., Flemming, F., Coulson, S., & Deschenes, C. (2012). Experimental investigation of draft tube inlet velocity field of a propeller turbine. *Journal of Fluids Engineering*, *134*(10), 101102.

Gagnon, J. M., F. Flemming, R. Qian, Desch, Aanes C, & Coulson, S. (2010). *Experimental and numerical investigations of inlet boundary conditions for a propeller turbine draft tube*. ASME, editor, 3rd Joint US-European Fluids Engineering Summer Meeting and 8th International Conference on Nanochannels, Microchannels, and Minichannels, Montreal.

Galvan, S., Reggio, M., & Guibault, F. (2011). Assessment study of k-e turbulence models and near-wall modeling for steady state swirling flow analysis in draft tube using fluent. *Engineering Applications of Computational Fluid Mechanics*, *5*(4), 459–478.

Gubin, M. F. (1973). *Draft tubes of hydroelectric stations*. New Delhi, India: Amerind Publishing.

Henau, V. D., Payette, F. A., Sabourin, M., Desch, Aanes C, Gagnon, J. M., & Gouin, P. (2010). Computational study of a low head draft tube and validation with experimental data. *IOP Conference Series: Earth and Environmental Science*, *12*(1), 012084.

Jonsson, P. P., Mulu, B. G., & Cervantes, M. J. (2012). Experimental investigation of a Kaplan draft tube -Part II: Off-design conditions. *Applied Energy*, *94*, 71–83.

Krzemianowski, Z., Banaszek, M., & Tesch, K. (2011). Experimental validation of numerical model within a flow configuration of the model Kaplan turbine. *Mechanics and Mechanical Engineering*, *15*, 297–307.

Kurosawa, S., & Satou, S. (2006). *Turbulent flow simulation for the draft tube of a Kaplan turbine*. 23rd IAHR Symposium on hydraulic machinery and systems. Yokohama, Japan: IAHR.

Liu, S., Shao, J., Wu, S., & Wu, Y. (2008). Numerical simulation of pressure fluctuation in Kaplan turbine. *Science in China Series E: Technological Sciences*, *51*(8), 1137–1148.

Marjavaara, D. B., Lundström, S. T., Wright, J., Kamakoti, R., Thakur, S., & Shyy, W. (2005). *Steady and unsteady simulations of the turbine-99 draft tube using cfx-5 and stream*. Proceedings of Turbine-99 III Sweden: Luleå University of Technology, number 2005:20.

Menter, F. R. (1992). Influence of freestream values on k − ω turbulence model predictions. *AIAA-Journal*, *30*, 6.

Menter, F. R. (1994). Two-equation eddy-viscosity models for engineering applications. *AIAA Journal*, *32*, 1598–1605.

Menter, F. R. (2003). Turbulence modelling for turbomachinery. *QNET-CFD Network Newsletter*, *2*, 10–13.

Mulu, B. G., & Cervantes, M. J. (2009). *Experimental investigation of a Kaplan model with LDA*. Proceedings of the 33th Congress of IAHR, Vancouver, Canada.

Mulu, B. G., Cervantes, M. J., Vu, T. C., Devals, C., & Guibault, F. (2011). *Effects of inlet boundary conditions on Kaplan draft tube simulation accuracy*. Proceedings of the Hydro 2011 Conference.

Mulu, B. G., Jonsson, P. P., & Cervantes, M. J. (2012). Experimental investigation of a Kaplan draft tube -Part I: Best efficiency point. *Applied Energy*, *94*, 71–83.

Nilsson, H. (2006, October). *Evaluation of OpenFOAM for CFD of turbulent flow in water turbines*. 23rd IAHR Symposium-Yokohama, Japan.

Nilsson, H., & Cervantes, M. J. (2012). Effects of inlet boundary conditions, on the computed flow in the turbine-99 draft tube, using OpenFOAM and CFX. *IOP Conference Series: Earth and Environmental Science, 15*(3), 032002.

Petit, O., Mulu, B. G., Nilsson, H., & Cervantes, M. J. (2010). Comparison of numerical and experimental results of the flow in the U9 Kaplan turbine model. *IOP Conference Series: Earth and Environmental Science, 12*(1), 012024.

Petit, O., Nilsson, H., Vu, T. C., Manole, O., & Leonsson, S. (2008). *The flow in the U9 Kaplan turbine -Preliminary and planned simulations using CFX and OpenFOAM*. Proceedings of the 24th Symposium on Hydraulic Machinery and Systems, IAHR.

Pope, S. B. (2000). *Turbulent flows*. Cambridge: Cambridge University Press.

Senoo, Y., & Nagata, T. (1972). Swirl flow in long pipes with different roughness. *Bulletin of the JSME, 15*(90), 1514–1521.

Su, W. T., Li, F. C., Li, X. B., Wei, X. Z., & Zhao, Y. (2012). Assessment of LES performance in simulating complex 3D flows in turbo-machines. *Engineering Applications of Computational Fluid Mechanics*, *6*(3), 356–365.

Vieser, W., Esch, T., & Menter, F. (2002). *Heat transfer predictions using advanced two-equation turbulence models* (Technical report). ANSYS Corp.

Vu, T. C., Devals, C., Zhang, Y., Nennemann, B., & Guibault, F. (2011a). Steady and unsteady flow computation in an elbow draft tube with experimental validation. *International Journal of Fluid Machinery and Systems, 4*(1), 87–96.

Vu, T. C., Koller, M., Gauthier, M., & Deschêne, C. (2011b). Flow simulation and efficiency hill chart prediction for a propeller turbine. *International Journal of Fluid Machinery and Systems*, *4*(2), 243–254.

Wilcox, D. C. (1993). *Turbulence modeling for CFD*. La Canada, CA: DCW Industries.

Yakhot, V., Orszag, S. A., Thangam, S., Gatski, T. B., & Speziale, C. G. (1992). Development of turbulence models for shear flows by a double expansion technique. *Physics of Fluids A, 4*(7), 1510–1520.